PCCP

PAPER

View Article Online
View Journal | View Issue

Cite this: *Phys. Chem. Chem. Phys.*, 2016, **18**, 3675

Static and dynamic electronic characterization of organic monolayers grafted on a silicon surface†

O. Pluchery,*[a] Y. Zhang,[bc] R. Benbalagh,[d] L. Caillard,[ae] J. J. Gallet,[d] F. Bournel,[d] A.-F. Lamic-Humblot,[f] M. Salmeron,[b] Y. J. Chabal[e] and F. Rochet[d]

Received 3rd October 2015,
Accepted 4th January 2016

DOI: 10.1039/c5cp05943g

www.rsc.org/pccp

Organic layers chemically grafted on silicon offer excellent interfaces that may open up the way for new organic–inorganic hybrid nanoelectronic devices. However, technological achievements rely on the precise electronic characterization of such organic layers. We have prepared ordered grafted organic monolayers (GOMs) on Si(111), sometimes termed self-assembled monolayers (SAMs), by a hydrosilylation reaction with either a 7-carbon or an 11-carbon alkyl chain, with further modification to obtain amine-terminated surfaces. X-ray photoelectron spectroscopy (XPS) is used to determine the band bending (~0.3 eV), and ultraviolet photoelectron spectroscopy (UPS) to measure the work function (~3.4 eV) and the HOMO edge. Scanning tunneling microscopy (STM) confirms that the GOM surface is clean and smooth. Finally, conductive AFM is used to measure electron transport through the monolayer and to identify transition between the tunneling and the field emission regimes. These organic monolayers offer a promising alternative to silicon dioxide thin films for fabricating metal–insulator–semiconductor (MIS) junctions. We show that gold nanoparticles can be covalently attached to mimic metallic nano-electrodes and that the electrical quality of the GOMs is completely preserved in the process.

Introduction

Molecular electronics offers new strategies for downscaling integrated circuit devices.[1] On the one hand, single-molecule experiments strive to investigate the fundamental phenomena when electrons are driven through a single molecule.[2–5] On the other hand, a layer of organic molecules can provide a unique connection to the existing silicon-based electronics, and be used to perform specific functions such as diodes, resonant tunnel diodes, memory devices or transistors. Unfortunately, the interface of silicon (Si) is often affected by oxidation and it is extremely challenging to prepare a silicon–molecule interface with tailored and defect-free electronic characteristics.[6–9] Even more challenging is to fabricate metal–insulator–semiconductor (MIS) junctions with an organic monolayer as the insulating layer.[10,11] In the past fifteen years, several chemical methods have been proposed for functionalizing silicon surfaces with highly ordered organic monolayers. Hydrosilylation involves the reaction of oxide-free, H-terminated Si surfaces with alkene functionality. This enables the grafting of alkyl chain molecules to form a stable Si–C bond using several different activation processes: thermal, catalytic, photochemical or radical.[12–16] The mechanisms at play for this reaction are now well established,[17–20] and the properties offered by such grafted organic monolayers (GOMs) are harvested for a number of applications. An alternative method, based on supercritical carbon dioxide, has also been used to prepare organic layers on oxide -free Si.[21,22] A few devices have already been proposed, based on GOM/Si heterostructures, such as organic memory devices,[23] ideal Schottky diodes,[9] organic photovoltaic solar cells,[24] biological sensors,[25,26] and double-tunnel junctions for Coulomb blockade.[27]

GOMs are highly ordered organic layers, in which structural homogeneity leads to spatially homogeneous electronic properties and well-defined band structures. For these sensitive applications, these ultrathin molecular layers have to meet several requirements: (1) chemical: to protect the silicon substrate from oxidation and minimize the formation of interface states especially

[a] *Sorbonne Universités, UPMC Univ Paris 06, CNRS-UMR 7588, Institut des NanoSciences de Paris, F-75005, Paris, France. E-mail: Olivier.pluchery@insp.jussieu.fr*
[b] *Materials Sciences Division, Lawrence Berkeley National Laboratory, Berkeley, CA 94720, USA*
[c] *Applied Science and Technology Graduate Program, University of California at Berkeley, Berkeley, CA 94720, USA*
[d] *Sorbonne Universités, UPMC Univ Paris 06, CNRS-UMR 7614, Laboratoire de Chimie Physique, Matière et Rayonnement, F-75005, Paris, France*
[e] *Laboratory for Surface and Nanostructure Modification, Department of Materials Science and Engineering, University of Texas at Dallas, 800 West Campbell Road, Dallas, Texas 75080, USA*
[f] *Sorbonne Universités, UPMC Univ Paris 06, CNRS-UMR 7197, Laboratoire de Réactivité de Surface, F-75005 Paris, France*

† Electronic supplementary information (ESI) available: Chemical preparation of the GOMs and of the gold nanoparticles, other STM and c-AFM images, calculation of the surface sensitivity of XPS, XPS Au 4f core-level spectra, additional UPS spectra, useful parameters for band bending calculations. See DOI: 10.1039/c5cp05943g

during post-processing steps, (2) dielectric: to function well as a rectifier, a Schottky barrier, a tunnel junction, and (3) linker: to connect another electrode (thin film or nanoscale electrode). In this context, it is crucial to precisely evaluate the work function, the amount of surface defects, band bending throughout the processing steps and ensure that they meet the expected electronic requirements.

Different molecules have been investigated in the last ten years, and the band diagram of the corresponding monolayers was established with X-ray photoemission spectroscopy (XPS), ultraviolet photoemission spectroscopy (UPS),[28–33] and Kelvin probe force microscopy (KPFM).[34,35]

In the present work we focus on two types of GOMs with different thicknesses that can each act as a tunnel junction. We also chemically post-modify the layer with an amine moiety, making it possible to attach gold nanoparticles, *i.e.* nanoscale electrodes, acting as a non-planar MIS junction. We have already shown that this structure exhibits Coulomb blockade under the tip of a scanning tunneling microscope (STM).[27,36] In the present study, we monitor the dependence of the main electric parameters of the interface (band bending, work function, LUMO edge) on each processing step of their chemical preparation. We also measure and describe the transport regime through these tunnel junctions by using conductive atomic force microscopy (c-AFM).

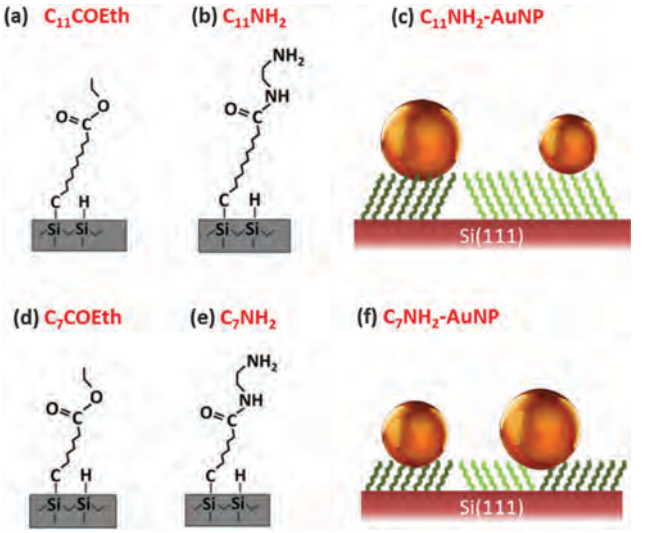

Fig. 1 Sketch of the six samples used in the present study. The molecules are closely packed and protect the Si(111) substrate against oxidation. Two alkyl chains were grafted (C7 and C11) and two terminations were prepared. Gold nanoparticles were deposited on the amine terminated surfaces.

Experimental section

Materials and methods

The samples are obtained from Si(111) monocrystals, n+ doped with a resistivity of 0.01 Ohm cm (a dopant concentration of 2×10^{18} cm^{-3}) and with a miscut of 0.5° in the $\langle \bar{1}\bar{1}2 \rangle$ direction. They are cut into 10×8 mm^2 pieces and prepared using wet chemical methods in a N_2-purged glovebox (amount of water and oxygen below 1 ppm) following a well-established protocol[12–16,20] described in our previous studies (see also ESI,† for additional details).[27,36,37] Briefly, the Si substrates are cleaned with a Piranha solution, then with an NH_4F solution to produce atomically flat, H-terminated Si(111) surfaces.[38] Next, two different alkene molecules (with different alkyl chain lengths) are used to synthesise grafted organic monolayers (GOMs) by hydrosilylation, denoted SiC_{11}-COEth and SiC_7-COEth (Fig. 1a and d). The long GOM, ethyl-undecylenate, is reacted with H-Si(111) by thermal hydrosilylation at 200 °C[37] while the short GOM, ethyl-heptenoate, is grafted by UV activation.[27] These two surfaces are terminated with an ester and can be modified following a two-step procedure. In the first step the ester is deprotected into a carboxylic moiety; in the second step, this termination is reacted with *N*-hydroxysuccinimyl (NHS) to obtain an amine. These two surfaces are depicted in Fig. 1b and e and termed SiC_{11}-NH_2 and SiC_7-NH_2. The amine group is essential to attach gold nanoparticles through direct amine–gold bonding. The fully reacted surfaces, with Au nanoparticles, remain stable enough in an Ar-filled plastic container for shipping from Texas to France (for XPS, STM and AFM characterization) and to California (for conductive AFM measurements).

Gold nanoparticles (AuNPs) are prepared as a colloidal solution from the reduction of $HAuCl_4$ by ascorbic acid[27,36,39,40] (details in the ESI†). The amine terminated surfaces are dipped into the colloidal solution for about 10 min after the solution was acidified at pH ~ 5. The amine is protonated, which enables the attachment of AuNPs. The surface density is measured with AFM and found to be 7×10^9 AuNP per cm^2.[27,36] TEM measurements have shown that the AuNPs are spherical and with an average diameter of 8.2 nm and a size dispersion of 4.0 nm, which allows Coulomb blockade experiments.[27,36] We estimate that 0.3% of the surface is covered with gold (average distance between AuNPs is 120 nm). The two AuNP-functionalized surfaces depicted in Fig. 1c and f are labeled $C_{11}NH_2$-AuNP and C_7NH_2-AuNP.

Instrumentation

STM was used to check the quality of the GOMs, performed in an UHV chamber (a base pressure of 3×10^{-11} mbar) after the surface was annealed in a vacuum at 150 °C for 30 min. This procedure removes the physisorbed molecules (mostly water) and stabilizes the STM imaging conditions. Importantly it does not alter the organic layer as revealed by infrared absorption measurements.[27,37]

X-Ray Photoelectron Spectroscopy (XPS) was carried out under UHV conditions and the core-level spectra were measured with a non-monochromatized Al Kα source ($h\nu$ = 1486.61 eV for the main Al $K\alpha_{1,2}$ line). The takeoff angle of the photoelectrons was normal to the surface. The overall energy resolution was 0.85 eV (source and analyzer). For UV photoemission spectroscopy (UPS) measurements, the UV source was the He I line ($h\nu$ = 21.21 eV) and a spectral resolution of 50 meV was achieved. Binding energies (BEs) and kinetic energies (KEs) are referenced with respect to the Fermi level. The Fermi edge is determined *via* UV photoemission spectroscopy of a freshly sputtered (unannealed)

polycrystalline gold foil. Work functions are determined by measuring the cutoff of the secondary electron edge (see below).

Conductive AFM measurements were performed in an UHV chamber (a base pressure of 5×10^{-9} torr) to measure the transport properties of the GOMs. The AFM measurements were carried out with a Cr/Pt tip on samples previously annealed for 30 min at 120 °C in a vacuum. Finally, AFM was also used in contact mode to record the topography of the samples and to record *I–V* data for selected points.

Results

Morphology of the GOM surface (STM)

Fig. 2 shows STM images of the C_7-NH_2 surface. This 100×100 nm^2 image remains stable, as expected for a compact and homogeneous GOM monolayer. The surface exhibits circular spots (the inset of Fig. 2) of typically 4 nm diameter due to small domains of molecules in which the C_7 alkyl chains are tilted in the same direction with respect to the surface, as schematically shown in Fig. 1c and f.

GOMs with long chain molecules, C_{11}-NH_2, also yield stable STM images similar to those in Fig. 2 (see ESI†), consistent with good molecular organization. The thickness of the amine-terminated monolayers, measured by ellipsometry, is 1.3 nm for C_7-NH_2 and 1.6 nm for C_{11}-NH_2.[27,37]

Estimation of the surface oxidation (XPS)

The XPS chemical analysis of C_7-NH_2 and C_{11}-NH_2 surfaces was essential for confirming the bonding of the organic layer as depicted in Fig. 1 and published earlier.[27,36] We focus now on analyzing the traces of oxide at the interface since they are responsible for most of the electronic surface defects. The Si 2p core-level spectra of three C_{11} GOMs are presented in Fig. 3. Under the present experimental conditions, photoelectrons probe *ca.* 3 nm below the surface (details of the calculation given in the ESI†). Deconvolution of the main spectral feature therefore includes the bulk contribution denoted B, and weaker surface components shifted +0.3 eV upwards and representing Si–C bonds.[42] The Si–H component, expected at +0.14 eV from B, is incorporated into the main peak.[43] Four Si oxidation states (+0.9 eV per O ligand) need to be considered as the samples were shortly exposed to air.[41] The intensity of these oxidation states is used to measure the impact of the successive treatments on the silicon wafer. For the C_{11}-COEth sample, the bulk line is at 99.50 eV and the sum of the four oxidation states Σ_{ox} corresponds to 9% of the spectral weight. It can be roughly interpreted as 9% of the silicon atoms being in an oxidized state. The 4th oxidation state 4+ (SiO_2) has a weight of only 1%. For the C_{11}-CNH_2 sample, the bulk line is at 99.57 eV, and $\Sigma_{ox} = 8\%$, similar to the C_{11}-COEth case, but the 4th oxidation state is now more visible (2%). Finally, after attaching the Au NPs (C_{11}-CNH_2-AuNP), the bulk line is at 99.63 eV and Σ_{ox} is equal to 11% (the 4th state weighs now 3%). While oxidation progresses slightly with each subsequent treatment, the attack is believed to be local (closer to "pitting", occurring at ill-protected spots) rather than homogeneous, and remains at an acceptably low level, even after oversea shipping. The Si $2p_{3/2}$ positions for the two types of GOMs are collected in Table 1. The Si $2p_{3/2}$ values found for the C_7 GOMs are very close to that found for the C_{11} one.

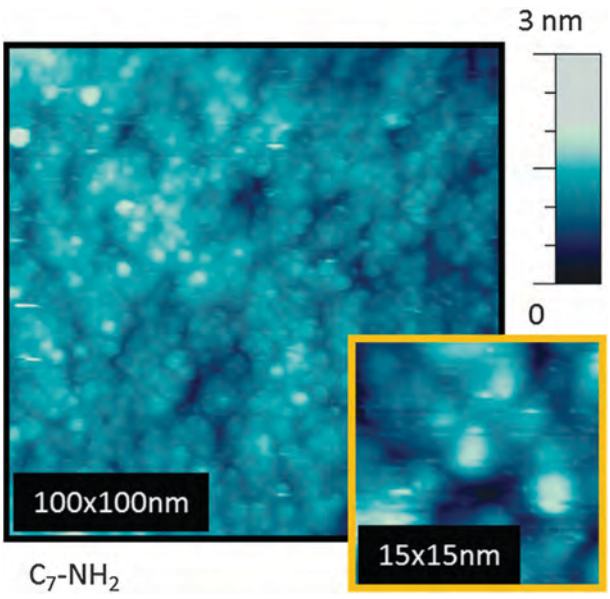

Fig. 2 STM image (100×100 nm) of the C_7-NH_2 molecular layer grafted on Si(111) recorded at room temperature under a sample bias of −2 V. The surface was annealed at 150 °C for 30 min before scanning. Molecules are organized in bundles of ~4 nm diameter (inset).

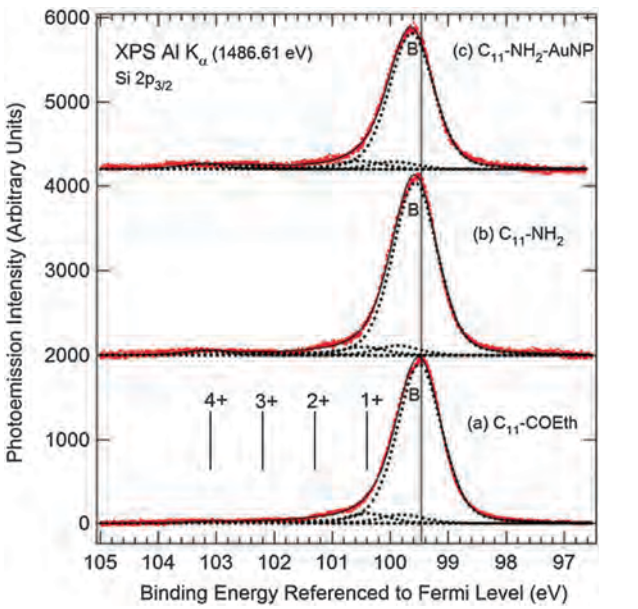

Fig. 3 Si $2p_{3/2}$ core-level peaks from XPS experiments (red dots) of the (a) C_{11}-COEth, (b) C_{11}-NH_2 and (c) C_{11}-NH_2AuNP grafted organic monolayers. Fits are made with sums of pseudo-Voigt curves (see text) and several contributions are highlighted. The main peak from the bulk is denoted B. The four oxidation states of silicon are indicated from 1+ to 4+. The position of peak B is used for measuring the surface band bending in our samples using the fact that the energy distance between the valence band maximum and the Si $2p_{3/2}$ binding energy is 98.74 eV.[41]

Table 1 Electronic properties measured for our six samples. BE(Si $2p_{3/2}$) (referenced to E_F) is used to compute $(E_F - E_{VBM})_S$, the (positive) band bending qV_{bb} and the surface charge density expressed in unit charge per Si atom (per mononolayer). (*) These values are averaged over the photoemission probing depth, the "true" qV_{bb} (n^S) values being slightly greater as explained in the ESI. The work function WF is obtained from the secondary electron edge cutoff (He I source). It is used to calculate the surface electronic affinity. The HOMO edge is also obtained from the valence band spectra (He I). Values for the electronic affinity are taken from (a) Akremi *et al.*[57] (b) Hunger *et al.*[58] (c) Hunger *et al.*[59] (d) Michaelson *et al.*[60] (e) Hollinger *et al.*[61]

Sample	BE(Si $2p_{3/2}$) (eV)	$(E_F - E_{VBM})_S$	qV_{bb} (eV)	n^S e$^-$/Si atom	WF (eV)	χ^s (eV)	HOMO edge (eV)
	Binding energy		Band bending*	Surface charge density*	Work function	Electronic affinity	
C_7-COEth	99.48	0.74	0.31	3.5×10^{-3}	3.58	3.20	4.91
C_{11}-COEth	99.49	0.75	0.30	3.5×10^{-3}	3.57	3.20	4.85
C_7-NH_2	99.55	0.81	0.24	3.1×10^{-3}	3.39	3.05	
C_{11}-NH_2	99.57	0.83	0.22	3.0×10^{-3}	3.03	2.74	5.11
C_7-NH_2-AuNP	99.59	0.85	0.20	2.8×10^{-3}	3.32	3.05	
C_{11}-NH_2-AuNP	99.63	0.89	0.16	2.5×10^{-3}	3.05	2.82	5.22
Si(111)-7 × 7						4.16[e]	
H-Si(111)						4.17[a,b]	
CH_3–Si(111)						3.7[c]	
Sputtered Au					5.0		
Au(111)					5.1[d]		

Surface band bending measurements (XPS)

Band bending is observed because electrically active defects are present at the surface.[44] Indeed, if the functionalization process could saturate every dangling bond, the surface would be electrically neutral, and the semiconductor would be under flat-band conditions. The presence of defects leads to the localization of charges at the surface (negative for n-type silicon or positive for p-type), and the formation of a space charge of opposite sign in Si. An electric field appears and the bands bend upward (n-type) or downward (p-type). The absolute position of Si $2p_{3/2}$ (peak B) is used to determine the surface band bending qV_{bb}, which can be written as:

$$qV_{bb} = (E_F - E_{VBM})_B - (E_F - E_{VBM})_S \quad (1)$$

The index B and S designates the bulk and surface, respectively, E_F is the Fermi level and E_{VBM} the silicon valence band maximum (see Scheme 1). $(E_F - E_{VBM})_B$ is calculated from the dopant concentration N_D and in the present case $(E_F - E_{VBM})_B$ = 1.05 eV. At the surface $(E_F - E_{VBM})_S$ is determined by the measurement of the BE of the Si $2p_{3/2}$ core level, BE(Si $2p_{3/2}$)^{meas} and the knowledge of the energy difference $(E_{VBM} - BE(Si\ 2p_{3/2}))$, which is constant and equal to 98.74 eV.[41] Then qV_{bb} can be written as:

$$qV_{bb} = (E_F - E_{VBM})_B - [BE(Si\ 2p_{3/2})^{meas} - (E_{VBM} - BE(Si\ 2p_{3/2}))] \quad (2)$$

Finally one gets:

$$qV_{bb} = 99.79\ eV - BE(Si\ 2p_{3/2})^{meas} \quad (3)$$

For example, for the C_{11}-COEth sample, the Si $2p_{3/2}$ BE is measured to be 99.49 eV and the Si bands were bent upwards by an amount qV_{bb} = +0.30 eV. Once the band bending is known, the surface charge density σ can be derived following the method shown by Sze:[45] $\sigma = \sqrt{2\varepsilon_0\varepsilon_{Si}qV_{bb}N_D}$, where ε_{Si} is the relative permittivity of Si, qV_{bb} is the band bending energy (in J) and N_D is the donor concentration in the semiconductor. Knowing that the Si atom surface density is 7.85×10^{14} atom per cm^2,[45] we can express σ in terms of the number of unit charges per Si surface atom n^S.

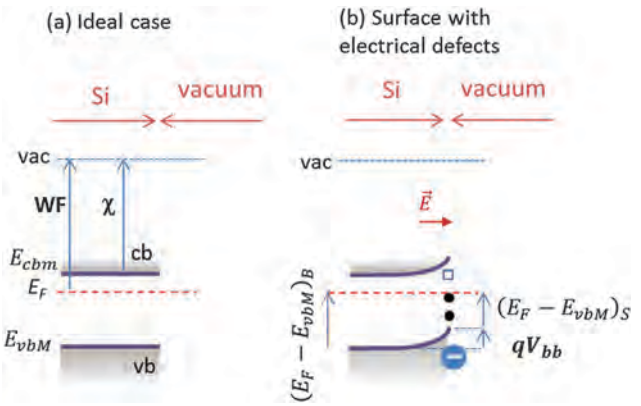

Scheme 1 Band diagram of an n-doped silicon surface. In the ideal case (a), when there are no interface states the conduction and valence bands (cb and vb respectively) are flat near the surface. WF is the work function (WF = 4.12 eV in our case), χ is the electronic affinity of the surface and the vacuum level is denoted *vac*. In the presence of electrically active surface states (b), the defects below the Fermi-level E_F are charged and the interface acquires a net negative charge. This charge transfer is compensated by an electric field. The surface band bending can be measured by comparing the measured value of $E_F - E_{VBM}$ to the bulk value.

The qV_{bb} and n^S values obtained for our different samples are collected in Table 1. All band bending values are *circa* +0.3 eV and for all terminations, n^S is in the range $\sim 3 \times 10^{-3}$ unit charges per Si atom, which corresponds to an amount of unit charge per surface area of 2.4×10^{12} e$^-$ cm^{-2}. For comparison, transport measurements were carried out with the mercury probe method on a similar Si/GOM interface prepared in our group with the same method. An interface state density as low as 1.6×10^{11} V^{-1} cm^{-2} was obtained, which corresponds to an interface density of $\sim 1 \times 10^{11}$ e$^-$ cm^{-2} at an applied bias of 0.5 V.[46,47] We observed 25 times more interface states in our case, possibly due to extra handling needed for these measurements.

To obtain a flat band situation, the areal density of defects should be at least one order of magnitude below this value.[48,49] The electrical defect is likely a triply coordinated silicon P_b-like defect,[50,51] with a double occupancy (Si^-) given the present high n-doping. As the σ Si–C bond does not introduce (bonding and antibonding) states in the gap, the origin of electrical defects is very likely related to the unintentional oxidation of the surface, which is hard to fully avoid during air exposure during the required transfer steps. We see no difference in qV_{BB} between the C_7-COEth and the C_{11}-COEth, which confirms that the two molecular layers have very similar structures despite the slightly different hydrosilylation processes (UV or thermal activation). Rather we observe a slight decrease in qV_{BB} (towards a flat band configuration) after NH_2 termination. Interestingly, gold nanoparticle deposition does not create new defects.

GOM electronic structure (UPS)

The UV photoelectron spectra of C_{11}-COEth and C_7-COEth GOMs are presented in Fig. 4. Note that He I emission is composed of a main line Iα at 21.21 eV and of a satellite Iβ, shifted to higher energy by 1.854 eV and representing 3% of the Iα intensity; therefore, the corresponding photoemission contribution is subtracted from the raw data for all the spectra in Fig. 4. Because the C 2p/Si 3p cross-section ratio is ~18.5 at $h\nu$ = 21.21 eV,[52] the UPS spectra are dominated by the contribution of the organic layer. The Highest Occupied Molecular Orbital (HOMO) of the organic layer appears in the steep decrease of the UPS signal on the right side of the spectra in Fig. 4. It is accompanied by a tail on its low binding energy side, which has previously been assigned to filled induced density of interface states (IDISs).[29] Typically, the tail extends up to 3.6–3.2 eV in the GOM gap. Nevertheless, the overall barrier height for electrons between the Si conduction band and the alkyl electronic levels is determined by the edges of the LUMO levels because these states extend throughout the alkyl chain, unlike the tails.[29] As shown in Fig. 4, we determine the HOMO edges graphically at the intersection of two lines, one for the HOMO edge and one for the gap state tail. The HOMO edge is ~4.9 eV below the Fermi level for C_{11}-COEth and for C_7-COEth (see also Table 1 for more data). This value is consistent with data obtained by Salomon on a very similar Si-$C_{12}H_{25}$ GOM on n-Si(111).[29,53] For the Si-C_{11} GOM, the addition of the NH_2 moiety only slightly shifts the HOMO edge to 5.1–5.2 eV.

Work function of the GOMs

The work function (WF) is by definition the energy difference between the vacuum level and E_F. It is obtained from the secondary electron edge (SE) curve measured with the He source, as follows:

$$\mathrm{WF} = h\nu + \mathrm{KE}_{\mathrm{cutoff}} - \mathrm{KE}_{\mathrm{Fermi}} \quad (4)$$

where KE_{Fermi} is the kinetic energy of the Fermi level (measured on a clean gold surface) when no bias is applied to the sample (see ESI,† for more details). The electron affinity χ is the energy difference between the vacuum level and the minimum of the conduction band E_{cbm}. It is an intrinsic property of the modified Si surface. The expression for χ is:

$$\chi = \mathrm{WF} - (E_{\mathrm{CBM}} - E_{\mathrm{F}}) = \mathrm{WF} - (E_{\mathrm{g}} - (E_{\mathrm{F}} - E_{\mathrm{VBM}})) \quad (5)$$

where E_g is the band gap (1.12 eV).

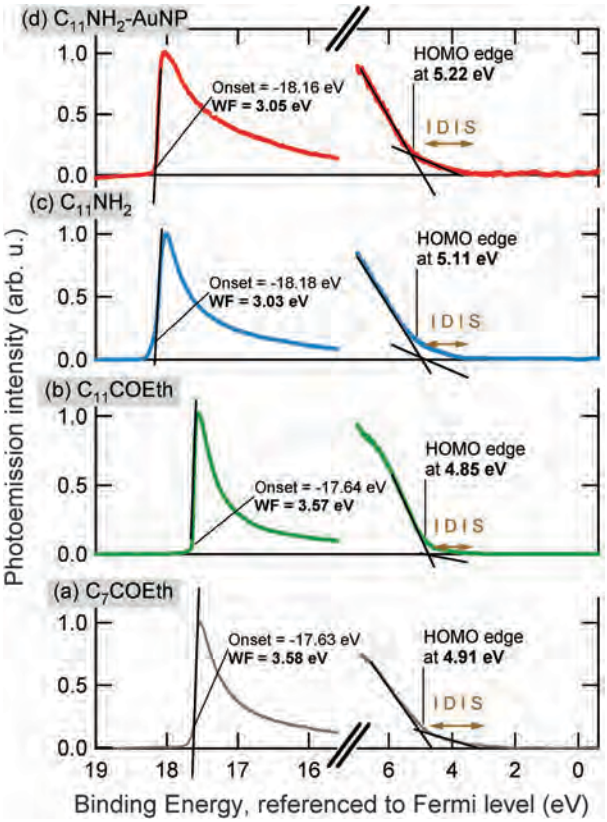

Fig. 4 Secondary electron (SE) edges (left part of the spectra) and valence UP Spectra (right spectra) of (a) C_7-COEth, (b) C_{11}-COEth, (c) C_{11}-NH_2, and (d) C_{11}-NH_2-AuNP. The cutoffs of the SE curves are indicated by the vertical bars and are used to calculate the work functions of the different organic monolayers. The edges of the UP Spectra correspond to the highest occupied molecular orbital (HOMO).

The secondary electron edges (the excitation source is the He lamp) are shown for all the samples in Fig. 4 and in Fig. S4 of the ESI.† As the KE scale is referenced to E_F, the position of the cutoff gives directly the WF. WF and electron affinity χ are given in Table 1. Note that the SE edges are very sensitive to the homogeneity of the surface. Indeed on a patchy surface the lower cutoff is the averaged cutoff of the different areas,[54] and the edge of the higher WF region can emerge as a distinct onset. The steepness of the cutoffs in Fig. 4 points to a good surface homogeneity. It should also be noted that C_{11}-COEth and C_7-COEth have the same WF and χ, indicating that there is no effect of the alkyl chain length on the work function in this case. This is in line with previous theoretical studies[55] as well as experiments with alkanethiols on gold,[56] showing that the WF is practically the same for molecules ranging from $CH_3(CH_2)_7SH$ to $CH_3(CH_2)_{17}SH$. The value of χ (~3.2 eV) is about 1 eV smaller than that of the H-terminated Si(111)-1 × 1 surface (~4.2 eV[57,58]). On H-terminated Si(001) surfaces, the attachment of an

octadecene GOM leads to a decrease in WF in the range 0.6–0.9 eV.[34] A DFT calculation on a ($CH_3(CH_2)_4$) GOM on Si(001) shows that the WF decrease is due to the substitution of Si–H by Si–C bonds and to the dipole of the polar groups (CH_3) within the molecule.[34] Note that χ is still 0.5 eV lower than that of Si(111) surfaces directly terminated by CH_3 (3.7 eV[34]), possibly due to the dipole (with a normal projection oriented outward) borne by the ethanoate.

Finally, the addition of the terminal amine moiety produces layers with WF (Fig. 4) and χ (Table 1) smaller than that of the original ethanoate GOM. This means that the projection of the dipole of the amine termination (oriented outward) is larger, in absolute value, than that of the ethanoate. However in stark contrast with the ethanoate GOMs, the WF decrease is much smaller for the "short" C_7NH_2 (−0.15 eV) than for the "long" $C_{11}NH_2$ (−0.48 eV) GOM. This strongly suggests that the amine termination process is much more efficient on the C_{11}-COEth than on the C_7-COEth GOM. A plausible explanation is that C_7 is less ordered than the C_{11} GOM, with ethanoate functionalities less available for reaction. This is consistent with the higher resistance of C_7-COEth against oxidation in air, compared to that of C_{11}COEth.[36]

GOM conductivity (conductive-AFM)

The electron transport through the GOM was measured using conductive-AFM in contact mode. A typical AFM image is shown in Fig. 5 over an area of 300 × 300 nm^2 taken on a C_7-NH_2 surface. A series of images was recorded with different values of sample bias (tip grounded) and the topography was found to be closely similar to that of Fig. 5a. It displays parallel structures that are 30 nm wide corresponding to atomic terraces of the Si(111) surfaces and consistent with the sample miscut ($\alpha = 0.5^\circ$ in the $\langle \bar{1}\bar{1}2 \rangle$ direction yielding ~35 nm wide terraces).[62] At 0 V bias, the RMS roughness of this functionalized surface is 1.3 nm (see ESI,† for another AFM image). The surface morphology remains unchanged even after scans with 8 V sample bias. Spectroscopic data were also recorded at various points of the surface and two of them are displayed in Fig. 5b (taken at spots indicated on the image).

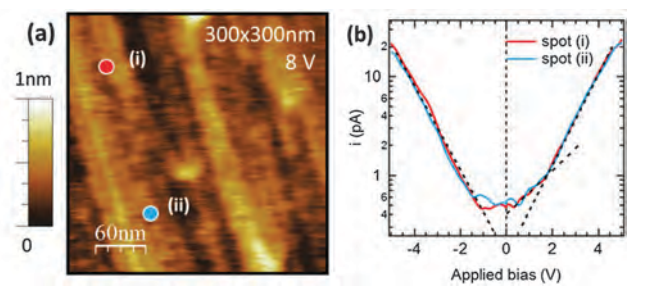

Fig. 5 (a) Topographic image (300 × 300 nm) obtained with conductive AFM, in contact mode for the C_7-NH_2 sample. A bias of 8 volt was applied to the sample while scanning. The parallel lines are terraces of the silicon substrate. (b) Spectroscopy curves acquired on the two spots marked on image (a). The curves are averaged over 10 sweeps. They show the two transport regimes discussed in the text.

Discussion

Surface dipole

The surface dipole is used to describe the energetic profile that a test charge undergoes when it crosses the interface. It is intrinsically linked to the electronic affinity and the work function of a surface. The formation of an ordered molecular layer creates a surface dipole layer that can either enhance or reduce the ability of extracting electrons from the surface. An electron coming from the bulk material will need more energy for crossing the interface if an inward oriented dipole is formed. The surface dipole energy $-e\delta$ is obtained as the difference between the actual electron affinity χ^S and the intrinsic silicon affinity χ^{Si}:

$$-e\delta = \chi^S - \chi^{Si} \quad (6)$$

where e is the absolute value of the elementary charge.

In eqn (6) a value of 4.05 eV is taken for χ^{Si}, as it is commonly used in evaluating Schottky barriers.[45]

The measured values for the molecular dipole energies presented in Table 2 lead to several conclusions. First, molecular grafting leads to negative dipole energies (all χ^S are smaller than χ^{Si}), corresponding to a dipole oriented outward. For all the GOMs studied here, the dipole energy has the same sign (negative) as those found for comparable organic layers. A comparison between SiC_7-COEth and SiC_{11}-COEth shows that the dipole energies are identical (δ = –0.85 eV). Actually it was shown that the potential drop occurs mostly because of the strong polarization of the Si–C bond.[34] The alkyl chain length has a more subtle effect on the WF that was discussed in detail by Fagas *et al.* whose conclusion supports our results of a limited difference in dipolar contribution between 7 and 11 carbon chain lengths.[55] However, further modification of SiC_7-COEth into SiC_7-NH_2 increases the absolute value of the dipole energy ($-e\delta$ = –1.0 eV). Calculations further confirm that an amine terminal group greatly contributes to the surface dipole.[55,63] What might be surprising at first glance is that the effect is still greater for SiC_{11}-NH_2 ($-e\delta$ = –1.31 eV) than for SiC_7-NH_2 ($-e\delta$ = –1.0 eV), although this is most likely due to the better ordering of the C_{11} alky chain compared to that of the C_7 one, ultimately leading to a denser layer.

Table 2 Comparison of the molecular surface dipole energies for different molecular functionalizations of the n-doped Si(111) surfaces. CH_3 is marked with an asterisk, because it binds to every silicon atom whereas in all the other surfaces the molecule replaces hydrogen for only half of the silicon surface atoms

Termination	C_7OEth	C_7NH_2	C_{11}OEth	$C_{11}NH_2$	H	CH_3*	C_5H_{11}	$C_{18}H_{37}$
Ref.	This work	This work	This work	This work	33	33	34	31
Dipole/eV	−0.85	−1.0	−0.85	−1.31	−0.07	−0.42	−0.6	−0.58

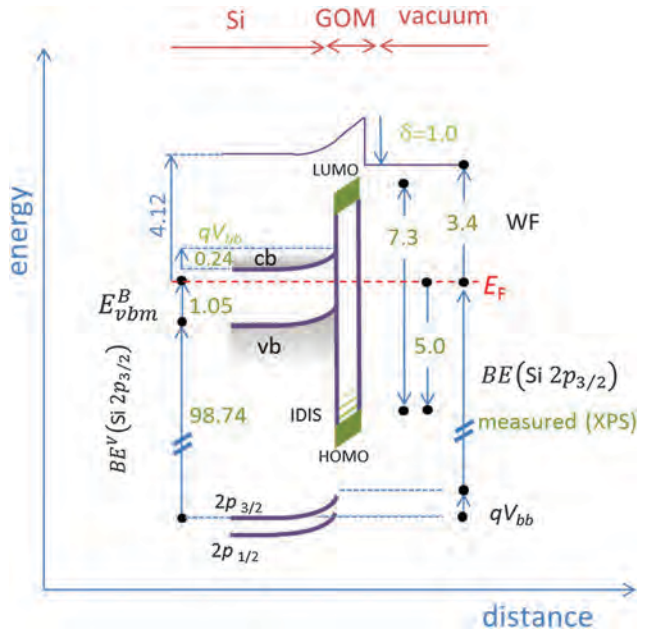

Scheme 2 Band diagram of the C_7-NH_2 sample, where an amine terminated molecule with a C_7 alkyl chain was grafted on Si(111). It forms a compact and homogeneous monolayer whose main electronic properties have been measured (values given in eV): the band bending, (E_{bb}), the work function (WF), the molecular dipole (δ), the position of the highest occupied molecular orbital below the Fermi level (HOMO). IDISs are induced density of interface states. Values are given in eV.

Band diagram of C_7-NH_2

Scheme 2 summarizes the positions of the SiC_7-NH_2 surface energy levels using values discussed previously (the other GOMs of the present study behave similarly and the values are summarized in Table 1). The value of the HOMO–LUMO gap was taken from data published elsewhere where the authors used IPES (Inverse Photo-Emission Spectroscopy) to evaluate the LUMO level.[29,53,64] For example the HOMO–LUMO gap of Si-$C_{10}H_{21}$ is evaluated to be 7.3 eV by Kahn's group, and their data show that the gap does not change more than 0.2 eV when the alkyl chain length is increased from C_6 to C_{18}. Therefore we retain the value of 7.3 eV for our GOMs. The band diagram represents the energy profile that an electron would feel when moving along the x axis. At around 15 nm away from the surface (depletion layer), it feels the upward band bending (0.24 eV), then crosses the tunnel barrier (the LUMO edge is at ~2.3 eV above the Fermi level) and is able to move out of the surface if its initial energy is greater than 3.4 eV above the Fermi level (definition of the work function). Moreover, we have shown that the presence of induced density of interface states (denoted IDISs in Scheme 2) strongly affects the transport through the molecular layer.

Modification of the surface electronic properties by dispersed AuNPs

The two amine-terminated surfaces decorated with 8 nm gold nanoparticles (C_7-NH_2-AuNP and C_{11}-NH_2-AuNP) have 0.3% of their surface covered with gold. This is a negligible amount when probed by spectroscopies that average over millimetric areas. Therefore, the influence of gold on the overall electronic surface properties is expected to be negligible (surface density below 10^{10} NP cm^{-2}) and this surface is used for checking how the chemical deposition of nanoparticles affects the global electronic properties of the GOMs. The work function values reported in Table 1 indicate that the WFs shift by only –0.07 eV and +0.02 eV upon deposition of AuNPs on C_7-NH_2 and C_{11}-NH_2, respectively. This demonstrates that the chemical treatment applied to the samples for depositing the metallic nanoparticles does not modify significantly the electronic properties of the GOMs. Moreover, the relatively low WFs obtained for the GOMs (<3.4 eV) compared to gold (5.1 eV) suggest that, at thermodynamic equilibrium, gold nanoparticles will spontaneously accumulate electrons which easily cross the tunnel barrier of the GOMs. This charging behavior was recently demonstrated with KPFM by measuring the charge state of individual nanoparticles of different sizes. For example a 10 nm nanoparticle accommodates five supplemental electrons.[65]

Transport behavior of the SiC_7-NH_2 surface

The band diagram presented in Scheme 2 provides the shape of the organic electric barrier when no bias is applied to the surface. When the metallic tip of the conductive-AFM is contacted to the layer (see Scheme 3a), the electrostatic equilibrium of the metal–insulator–semiconductor (MIS) structure changes.[45] The application of an external bias further modifies the structure, which needs to be addressed for understanding the electronic transport mechanism. Electronic transport through molecular layers is controlled by two parallel active mechanisms: the Schottky barrier inside the semiconductor caused by the band bending near the interface, and the tunnel barrier formed by the organic insulator. From the electrostatic values evaluated above, the profile of the band diagram was drawn numerically using the freely available software designed by Knowlton and Southwick.[66,67] Scheme 3a shows that, at zero bias when the AFM tip is in contact with the molecular surface, the silicon bands bend upward (inversion regime). The depletion layer spans over 20 nm. When a moderate positive voltage is applied to the semiconductor (*e.g.*, when the AFM tip is grounded), the transport occurs by tunneling through the molecular barrier. Scheme 3c shows that the electrons have to cross a trapezoidal barrier, in which case the transport is described by[45,68–71]

$$I \propto V \exp\left(-\frac{2d\sqrt{2m^*\phi}}{\hbar}\right) \quad (7)$$

where d is the barrier thickness, m^* is the electron effective mass, and ϕ is the barrier height.

However, when the bias is strongly increased (positive bias), the electric field across the GOMs becomes important and the electrons face a triangular barrier. The transport starts being dominated by field emission (Fowler–Nordheim regime), as depicted in Scheme 3c and d, and the current–voltage follows the relationship (positive bias):[68]

$$I \propto V^2 \exp\left(-\frac{4d\sqrt{2m^*\phi^3}}{3\hbar qV}\right) \quad (8)$$

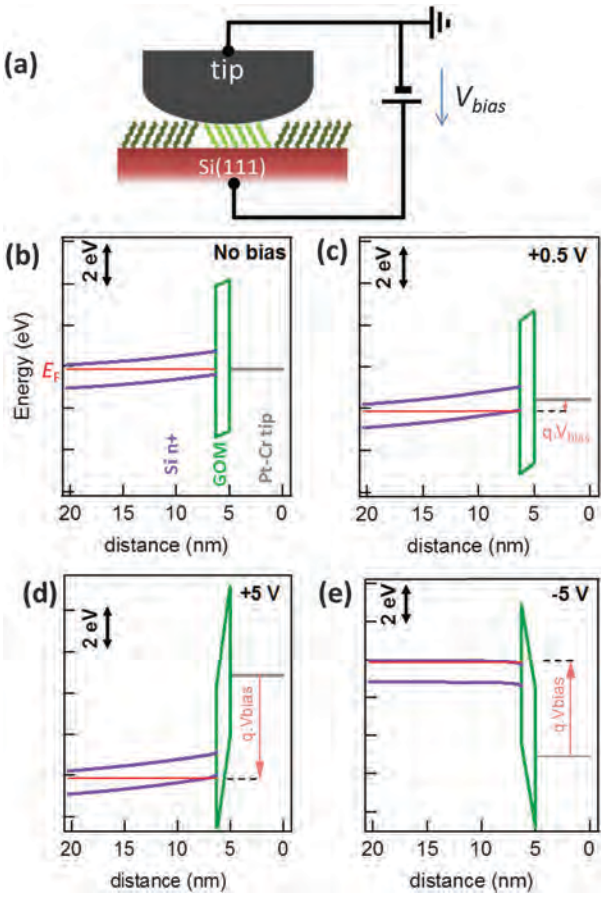

Scheme 3 Band diagram drawn when the tip of the conductive AFM is in contact with the Si-C_7NH_2 GOM (a). Calculations are done with the parameters discussed above. At zero sample bias (b) the silicon is already in inversion. With moderate sample bias (+0.5 V (c)) the barrier is trapezoidal (tunneling regime) whereas at strong bias (d and e) the barrier is triangular and the transport is dominated by thermionic emission.

A Fowler–Nordheim plot is the graph of $\ln(I/V^2)$ against I/V and is given in Fig. 6. From eqn (7), it obvious that $\ln\left(\frac{I}{V^2}\right) \propto \frac{1}{V} - 2\frac{d}{\hbar}\sqrt{2m^*\phi}$ for a tunneling regime and therefore we expect a linear evolution with a positive slope. This tunneling regime is identified in Fig. 6 for biases comprised between −2.2 V and 1.9 V (large values of $1/V$). On the other hand, eqn (8) shows that a linear evolution is also expected for strong positive biases, but with a negative slope. This trend is confirmed by our experiments for values of $1/V$ smaller than 1/1.9 Volt^{-1}. Fig. 6 clearly shows the transition between the tunneling and the field emission regimes, corresponding to the minima at −2.2 and +1.9 V. Moreover, the intersection with the vertical axis occurs at $-2\frac{d}{\hbar}\sqrt{2m^*\phi}$ for the low bias regime and the barrier height ϕ can be evaluated (with d = 1.3 nm and m^* = $0.25m_e$[53]). For positive bias, we calculate ϕ = 0.06 eV. From the simplified diagram of Scheme 3c, we expect a value of ∼2.5 eV. The discrepancy between the experimental and calculated values points to the complex transport mechanism. It shows that the

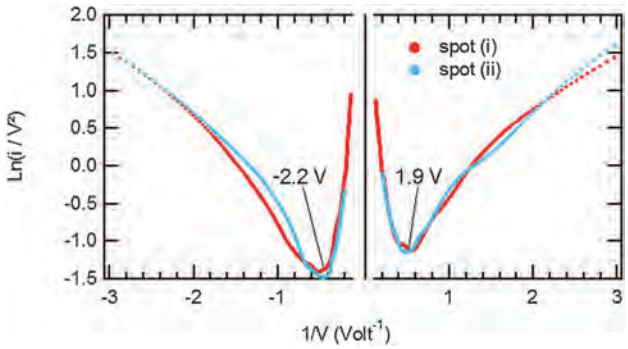

Fig. 6 Fowler–Nordheim plot where the transition between the tunneling regime (low bias regime) and the field emission (high bias) regime appears as a minimum in the graph. The two curves correspond to the two spots identified in Fig. 5.

induced density of interfaces states detected by our UPS spectra provide additional low energy paths for the electron to cross the tunnel barrier. Moreover the simplified diagram of Scheme 3 is calculated for a planar MIS structure, whereas the tip of the AFM cannot be represented with an infinite plane. The curvature will decrease the amount of band bending and therefore also the overall barrier height. The consideration of all these parameters exceeds the scope of the present study.

Conclusion

The complete energy diagram was derived for six organic alkyl-chain monolayers directly grafted on oxide-free, atomically flat H-terminated Si(111) surfaces. As shown by XPS, the GOMs clearly provide a barrier to oxidation and other chemical reactions during subsequent chemical processes: replacement of ethanoate by the amine head, AuNP deposition, and inevitable exposure to air. We established and analyzed in detail the band bending diagram of the GOMs on silicon and used it to explain the electronic transport properties of the GOMs. The conclusions derived from this work demonstrate that the surfaces functionalized by hydrosilylation are among the best candidates for building tailored hybrid nano-devices where the organic monolayers provide the electrically active layer. As theoreticians start providing methods for optimizing *a priori* the band diagram of a grafted organic monolayer[72] and other experimental studies continue to develop new approaches for fabricating MIS structures with organic monolayers,[73] GOMs will likely become essential components for the next generation nano-electronic devices.

Acknowledgements

L. C. acknowledges support by NSF-CHE (1300180), a Chateaubriand Fellowship and a Nanotwinning FP7 grant, NN294952. Y. Z. and M. S. acknowledge support by the "Self-Assembly of Organic/Inorganic Nanocomposite Materials" program, Office of Science, the Office of Basic Energy Sciences (BES), Materials Sciences and Engineering (MSE) Division of the U.S. Department of Energy (DOE) under Contract No. DE-AC02-05CH11231. It used

resources of the Molecular Foundry, a DOE Office of Science user facility.

Notes and references

1 J. C. Cuevas and E. Scheer, *Molecular Electronics*, World Scientific Publishing Company, London, 2010.
2 M. Ratner, *Nat. Nano*, 2013, **8**, 378–381.
3 L. Sun, Y. A. Diaz-Fernandez, T. A. Gschneidtner, F. Westerlund, S. Lara-Avila and K. Moth-Poulsen, *Chem. Soc. Rev.*, 2014, **43**, 7378–7411.
4 G. Comtet, G. Dujardin, L. Hellner, M. Lastapis, M. Martin, A. Mayne and D. Riedel, *Philos. Trans. R. Soc., A*, 2004, **362**, 1217–1226.
5 A. Y. Anagaw, R. A. Wolkow and G. A. DiLabio, *J. Phys. Chem. C*, 2008, **112**, 3780–3784.
6 S. F. Bent, *Surf. Sci.*, 2002, **500**, 879–903.
7 S. Lenfant, D. Guerin, F. T. Van, C. Chevrot, S. Palacin, J. P. Bourgoin, O. Bouloussa, F. Rondelez and D. Vuillaume, *J. Phys. Chem. B*, 2006, **110**, 13947–13958.
8 A. Vilan, O. Yaffe, A. Biller, A. Salomon, A. Kahn and D. Cahen, *Adv. Mater.*, 2010, **22**, 140–159.
9 R. Har-Lavan, O. Yaffe, P. Joshi, R. Kazaz, H. Cohen and D. Cahen, *AIP Adv.*, 2012, **2**, 012164.
10 K. Uosaki, H. Fukumitsu, T. Masuda and D. Qu, *Phys. Chem. Chem. Phys.*, 2014, **16**, 9960–9965.
11 A. B. Fadjie-Djomkam, S. Ababou-Girard and C. Godet, *J. Appl. Phys.*, 2012, **112**, 113701.
12 J. Terry, M. R. Linford, C. Wigren, R. Cao, P. Pianetta and C. E. D. Chidsey, *Appl. Phys. Lett.*, 1997, **71**, 1056–1058.
13 R. L. Cicero, M. R. Linford and C. E. D. Chidsey, *Langmuir*, 2000, **16**, 5688–5695.
14 O. Seitz, T. Boecking, A. Salomon, J. J. Gooding and D. Cahen, *Langmuir*, 2006, **22**, 6915–6922.
15 L. C. P. M. de Smet, A. V. Pukin, Q.-Y. Sun, B. J. Eves, G. P. Lopinski, G. M. Visser, H. Zuilhof and E. J. R. Sudhölter, *Appl. Surf. Sci.*, 2005, **252**, 24–30.
16 A. Faucheux, A. C. Gouget-Laemmel, C. Henry de Villeneuve, R. Boukherroub, F. Ozanam, P. Allongue and J. N. Chazalviel, *Langmuir*, 2006, **22**, 153–162.
17 S. Fellah, R. Boukherroub, F. Ozanam and J. N. Chazalviel, *Langmuir*, 2004, **20**, 6359–6364.
18 R. Boukherroub, *Curr. Opin. Solid State Mater. Sci.*, 2005, **9**, 66–72.
19 Y. Li, S. Calder, O. Yaffe, D. Cahen, H. Haick, L. Kronik and H. Zuilhof, *Langmuir*, 2012, **28**, 9920–9929.
20 P. Thissen, O. Seitz and Y. J. Chabal, *Prog. Surf. Sci.*, 2012, **87**, 272–290.
21 S. R. Puniredd, O. Assad, T. Stelzner, S. Christiansen and H. Haick, *Langmuir*, 2011, **27**, 4764–4771.
22 S. R. Puniredd, S. Jayaraman, S. H. Yeong, C. Troadec and M. P. Srinivasan, *J. Phys. Chem. Lett.*, 2013, **4**, 1397–1403.
23 S. Lee, J. Lee, H. Lee, Y. J. Yuk, M. Kim, H. Moon, J. Seo, Y. Park, J. Y. Park, S. H. Ko and S. Yoo, *Org. Electron.*, 2013, **14**, 3260–3266.
24 O. Yaffe, T. Ely, R. Har-Lavan, D. A. Egger, S. Johnston, H. Cohen, L. Kronik, A. Vilan and D. Cahen, *J. Phys. Chem. C*, 2013, **117**, 22351–22361.
25 F. Wei, B. Sun, Y. Guo and X. Zhao, *Biosens. Bioelectron.*, 2003, **18**, 1157–1163.
26 W. Cai, J. Peck, D. Van der Weide and R. Hamers, *Biosens. Bioelectron.*, 2004, **19**, 1013–1019.
27 L. Caillard, O. Seitz, P. Campbell, R. Doherty, A.-F. Lamic-Humblot, E. Lacaze, Y. J. Chabal and O. Pluchery, *Langmuir*, 2013, **29**, 5066–5073.
28 H. Haick, J. Ghabboun, O. Niitsoo, H. Cohen, D. Cahen, A. Vilan, J. Y. Hwang, A. Wan, F. Amy and A. Kahn, *J. Phys. Chem. B*, 2005, **109**, 9622–9630.
29 L. Segev, A. Salomon, A. Natan, D. Cahen, L. Kronik, F. Amy, C. K. Chan and A. Kahn, *Phys. Rev. B: Condens. Matter Mater. Phys*, 2006, **74**, 165323.
30 F. Thieblemont, O. Seitz, A. Vilan, H. Cohen, E. Salomon, A. Kahn and D. Cahen, *Adv. Mater.*, 2008, **20**, 3931.
31 C. A. Hacker, *Solid-State Electron.*, 2010, **54**, 1657–1664.
32 J. J. Gallet, F. Bournel, F. Rochet, U. Köhler, S. Kubsky, M. G. Silly, F. Sirotti and D. Pierucci, *J. Phys. Chem. C*, 2011, **115**, 7686–7693.
33 D. C. Gleason-Rohrer, B. S. Brunschwig and N. S. Lewis, *J. Phys. Chem. C*, 2013, **117**, 18031–18042.
34 I. Magid, L. Burstein, O. Seitz, L. Segev, L. Kronik and Y. Rosenwaks, *J. Phys. Chem. C*, 2008, **112**, 7145–7150.
35 Y. Zhang, D. Ziegler and M. Salmeron, *ACS Nano*, 2013, **7**, 8258–8265.
36 L. Caillard, S. Sattayaporn, A.-F. Lamic-Humblot, S. Casale, P. Campbell, Y. J. Chabal and O. Pluchery, *Nanotechnology*, 2015, **26**, 065301.
37 D. Aureau, Y. Varin, K. Roodenko, O. Seitz, O. Pluchery and Y. J. Chabal, *J. Phys. Chem. C*, 2010, **114**, 14180–14186.
38 G. S. Higashi, Y. J. Chabal, G. W. Trucks and K. Raghavachari, *Appl. Phys. Lett.*, 1990, **56**, 656–658.
39 E. C. Stathis and A. Fabrikanos, *Chem. Ind.*, 1958, 860–861.
40 J. Kimling, M. Maier, B. Okenve, V. Kotaidis, H. Ballot and A. Plech, *J. Phys. Chem. B*, 2006, **110**, 15700–15707.
41 F. J. Himpsel, G. Hollinger and R. A. Pollak, *Phys. Rev. B: Condens. Matter Mater. Phys*, 1983, **28**, 7014–7018.
42 L. J. Webb, D. J. Michalak, J. S. Biteen, B. S. Brunschwig, A. S. Y. Chan, D. W. Knapp, H. M. Meyer, E. J. Nemanick, M. C. Traub and N. S. Lewis, *J. Phys. Chem. B*, 2006, **110**, 23450–23459.
43 K. Hricovini, R. Günther, P. Thiry, A. Taleb-Ibrahimi, G. Indlekofer, J. E. Bonnet, P. Dumas, Y. Petroff, X. Blase, X. Zhu, S. G. Louie, Y. J. Chabal and P. A. Thiry, *Phys. Rev. Lett.*, 1993, **70**, 1992–1995.
44 Y. Zhang, D. Zherebetskyy, N. D. Bronstein, S. Barja, L. Lichtenstein, D. Schuppisser, L.-W. Wang, A. P. Alivisatos and M. Salmeron, *Nano Lett.*, 2015, **15**, 3249–3253.
45 S. M. Sze, *Physics of Semiconductor Devices*, John Wiley & Sons, New York, 2nd edn, 1981.
46 W. Peng, O. Seitz, R. A. Chapman, E. M. Vogel and Y. J. Chabal, *Appl. Phys. Lett.*, 2012, **101**, 051605.
47 The work function of mercury is 4.5 eV, therefore the system studied by Peng *et al.* is flatband at zero applied bias.

To obtain similar band bending as in our case, and compare the interface state density we use their D_{it} value at 0.3 V which is 1.6×10^{11} interface state per volt and per cm^2.
48 A. Zur, T. C. McGill and D. L. Smith, *Phys. Rev. B: Condens. Matter Mater. Phys*, 1983, **28**, 2060–2067.
49 F. J. Himpsel, B. S. Meyerson, F. R. M. Feely, J. F. Morar, A. Taleb-Ibrahimi and J. A. Yarmoff, *Varenna*, 1988.
50 P. J. Caplan, E. H. Poindexter, B. E. Deal and R. R. Razouk, *J. Appl. Phys.*, 1979, **50**, 5847–5854.
51 P. Broqvist, A. Alkauskas and A. Pasquarello, *Phys. Rev. B: Condens. Matter Mater. Phys*, 2008, **78**, 075203.
52 J. J. Yeh and I. Lindau, *At. Data Nucl. Data Tables*, 1985, **32**, 1–155.
53 A. Salomon, T. Boecking, O. Seitz, T. Markus, F. Amy, C. Chan, W. Zhao, D. Cahen and A. Kahn, *Adv. Mater.*, 2007, **19**, 445–450.
54 N. Bundaleski, J. Trigueiro, A. G. Silva, A. M. C. Moutinho and O. M. N. D. Teodoro, *J. Appl. Phys.*, 2013, **113**, 183720.
55 H. H. Arefi, M. Nolan and G. Fagas, *J. Phys. Chem. C*, 2015, **119**, 11588–11597.
56 D. M. Alloway, M. Hofmann, D. L. Smith, N. E. Gruhn, A. L. Graham, R. Colorado, V. H. Wysocki, T. R. Lee, P. A. Lee and N. R. Armstrong, *J. Phys. Chem. B*, 2003, **107**, 11690–11699.
57 A. Akremi, J. P. Lacharme and C. A. Sébenne, *Surf. Sci.*, 1998, **402–404**, 746–750.
58 R. Hunger, C. Pettenkofer and R. Scheer, *J. Appl. Phys.*, 2002, **91**, 6560–6570.
59 R. Hunger, R. Fritsche, B. Jaeckel, W. Jaegermann, L. J. Webb and N. S. Lewis, *Phys. Rev. B: Condens. Matter Mater. Phys*, 2005, **72**, 045317.
60 H. B. Michaelson, *J. Appl. Phys.*, 1977, **48**, 4729–4733.
61 G. Hollinger and F. J. Himpsel, *J. Vac. Sci. Technol., A*, 1983, **1**, 640.
62 For a given sample miscut α, the width of terraces a is expected to be 35 nm, since $a = h/\tan\alpha$, where h is the height of Si(111) step (h = 0.313 nm). This relatively high miscut was not intentional and results from the batch of wafers used for these experiments.
63 H. H. Arefi and G. Fagas, *J. Phys. Chem. C*, 2014, **118**, 14346–14354.
64 S. Avasthi, Y. Qi, G. K. Vertelov, J. Schwartz, A. Kahn and J. C. Sturm, *Surf. Sci.*, 2011, **605**, 1308–1312.
65 Y. Zhang, O. Pluchery, L. Caillard, A.-F. Lamic-Humblot, S. Casale, Y. J. Chabal and M. Salmeron, *Nano Lett.*, 2015, **15**, 51–55.
66 R. G. Southwick and W. B. Knowlton, *IEEE Trans. Device Mater. Reliab.*, 2006, **6**, 136–145.
67 B. Knowlton, http://nano.boisestate.edu/research-areas/multi-dielectric-energy-band-diagram-program/.
68 J. M. Beebe, B. Kim, J. W. Gadzuk, C. Daniel Frisbie and J. G. Kushmerick, *Phys. Rev. Lett.*, 2006, **97**, 026801.
69 S. Y. Sayed, J. A. Fereiro, H. Yan, R. L. McCreery and A. J. Bergren, *Proc. Natl. Acad. Sci. U. S. A.*, 2012, **109**, 11498–11503.
70 H. Hamoudi, K. Uosaki, K. Ariga and V. A. Esaulov, *RSC Adv.*, 2014, **4**, 39657–39666.
71 A. Salomon, T. Boecking, C. K. Chan, F. Amy, O. Girshevitz, D. Cahen and A. Kahn, *Phys. Rev. Lett.*, 2005, **95**, 266807.
72 B. Kretz, D. A. Egger and E. Zojer, *Adv. Sci.*, 2015, **2**, 1400016.
73 L. M. Ballesteros, S. Martín, J. Cortés, S. Marqués-González, F. Pérez-Murano, R. J. Nichols, P. J. Low and P. Cea, *Adv. Mater. Interfaces*, 2014, **1**, 1400128.

Static and Dynamic Electronic Characterization of Organic Monolayers Grafted on a Silicon Surface

Citation:

Pluchery, O., Y. Zhang, R. Benbalagh, L. Caillard, et al. 2016. "Static and dynamic electronic characterization of organic monolayers grafted on a silicon surface." Physical Chemistry Chemical Physics 18(5), doi:10.1039/c5cp05943g.